

# ADMM-Net: A Deep Learning Approach for Compressive Sensing MRI

Yan Yang, Jian Sun\*, Huibin Li, and Zongben Xu

**Abstract**—Compressive sensing (CS) is an effective approach for fast Magnetic Resonance Imaging (MRI). It aims at reconstructing MR images from a small number of under-sampled data in  $k$ -space, and accelerating the data acquisition in MRI. To improve the current MRI system in reconstruction accuracy and speed, in this paper, we propose two novel deep architectures, dubbed ADMM-Nets in basic and generalized versions. ADMM-Nets are defined over data flow graphs, which are derived from the iterative procedures in Alternating Direction Method of Multipliers (ADMM) algorithm for optimizing a general CS-based MRI model. They take the sampled  $k$ -space data as inputs and output reconstructed MR images. Moreover, we extend our network to cope with complex-valued MR images. In the training phase, all parameters of the nets, e.g., transforms, shrinkage functions, etc., are discriminatively trained end-to-end. In the testing phase, they have computational overhead similar to ADMM algorithm but use optimized parameters learned from the data for CS-based reconstruction task. We investigate different configurations in network structures and conduct extensive experiments on MR image reconstruction under different sampling rates. Due to the combination of the advantages in model-based approach and deep learning approach, the ADMM-Nets achieve state-of-the-art reconstruction accuracies with fast computational speed.

**Index Terms**—CS-MRI, deep learning, ADMM, discriminative learning, ADMM-Net.

## 1 INTRODUCTION

COMPRESSIVE sensing (CS), which aims at recovering a signal allowing for data sampling rate much lower than Nyquist rate, is a popular approach in the fields of signal processing and machine learning [1]. Nowadays, the CS method has been introduced for magnetic resonance imaging (MRI), leading to one of the most successful CS application, which is called compressive sensing MRI (CS-MRI) [2]. MRI is a non-invasive and widely used imaging technique providing both functional and anatomical information for clinical diagnosis, including data acquisition and image reconstruction processing. Imaging quality greatly affects the subsequent image analysis and processing which are useful for both doctors and computers. However, long scanning and waiting time may result in motion artifacts and patients' disamenity. All these facts imply that imaging speed for MRI is a fundamental challenge. CS-MRI methods handle this problem by reconstructing high quality MR images from a few sampling data in  $k$ -space (i.e., Fourier space), which reduces the scanning time significantly.

Generally, CS-MRI is formulated as a penalized inverse problem, and the solution to the problem is taken as the reconstructed MR image [2], [3]. Regularization of the model related to the data prior is a key component in a CS-MRI model to improve imaging precision. According to the CS theory, signal sparsity is an important prior to remove the aliasing artifacts due to undersampling in  $k$ -space [3]. In this way, sparse regularization can be explored

in specific transform domain [3], [4] or general dictionary-based subspace [5] to either achieve a higher acceleration factor or to improve the reconstruction performance. The corresponding sparse regularization is usually defined by  $l_q$  ( $q \in [0, 1]$ ) regularizer. In addition to the sparse representation of the image, nonlocal similarity property of images is also widely utilized in CS-MRI models [6], [7]. To improve the reconstruction quality, the combination of both local and nonlocal information is investigated in [8]. All of these approaches determine the formulation of sparse representation and sparse regularization by personal experiences, which is usually sub-optimal considering the requirements of quality and speed for MRI reconstruction. In summary, it is still a challenging task in CS-MRI to choose optimal transform domain / subspace and the corresponding regularization.

To optimize a CS-MRI model, there are three types of algorithms including gradient-based algorithm [3], variable splitting algorithm [9], [10], [11] and operator splitting algorithm [12]. Alternating Direction Method of Multipliers (ADMM) is a widely utilized variable splitting algorithm in CS-MRI, which has been proven to be efficient and generally applicable with convergence guarantee [13], [14]. It considers the augmented Lagrangian function of a given CS-MRI model, and splits variables into subgroups, which can be alternatively optimized by solving a few simple subproblems. Although ADMM is generally efficient for optimization, it is also not trivial to determine the optimal parameters (e.g., update rates, penalty parameters) influencing the reconstruction accuracy and speed in CS-MRI.

Recently, deep neural networks owing to strong learning ability from data have achieved exciting successes for image classification and segmentation [15], [16]. Moreover, regression-type deep networks provide state-of-the-art performance in image denoising and super-resolution as

• The authors are with the Institute for Information and System Sciences, School of Mathematics and Statistics, Xi'an Jiaotong University, Xi'an, 710049, China.  
E-mail: yangyan92@stu.xjtu.edu.cn, {jiansun,huibinli,zbxu}@mail.xjtu.edu.cn.

Manuscript received xxx, xxx; revised xxx, xxx.

well [17], [18]. In this work, we are interested in bridging the deep learning approach and inverse problem of compressive sensing with application in MR image reconstruction.

In this paper, we design two effective deep architectures inspired by ADMM algorithm optimizing a CS-MRI model to reconstruct high-quality MR images from under-sampled  $k$ -space data. We first define a deep architecture represented by a data flow graph, which derived from the ADMM iterative procedures for optimizing a general CS-MRI model. The operations in ADMM are represented as graph nodes, and the data flow between two operations is represented by a directed edge. Then we generalize this data flow graph to two different deep networks, dubbed *Basic-ADMM-Net* and *Generic-ADMM-Net* inspired by two different versions of ADMM algorithm. Furthermore, we extend our network to cope with the complex-valued MR image, dubbed *Complex-ADMM-Net*. These deep networks consist of multiple stages, each of which corresponds to an iteration in ADMM algorithm. Given an under-sampled  $k$ -space data, it flows over the network and outputs a reconstructed MR image. All the parameters (e.g., image transforms, shrinkage functions, penalty parameters, update rates, etc.) in the deep networks can be discriminatively learned from training pairs of under-sampled data in  $k$ -space and reconstructed image using fully sampled data by L-BFGS optimization and back-propagation [19] over the deep architectures. All the experiments demonstrate that the proposed deep networks are effective both in reconstruction accuracy and speed.

The main contributions of this study can be summarized as follows.

- We propose two novel deep ADMM-Nets by reformulating the ADMM algorithms solving a general CS-MRI model to deep networks for CS-MRI. The parameters in the CS-MRI model and the ADMM algorithm are all discriminatively learned from data.
- Extensive experiments show that the ADMM-Nets achieve state-of-the-art accuracy in MR image reconstruction with fast computational speed.
- Our proposed ADMM-Nets naturally combine the merits of traditional CS-MRI model and deep learning approach, which can be potentially applied to other inverse problems, such as image deconvolution, general compressive sensing applications.

The preliminary version of this work has been presented earlier in a conference [20]. This paper extends the initial version from several aspects to advance our approach. First, we generalize the ADMM-Net to a more general network structure (i.e., *Generic-ADMM-Net*) achieving higher MR image reconstruction quality. Second, we extend the network to reconstruct the complex-valued MR image which is more useful in clinical diagnosis. Third, we extensively evaluate the ADMM-Nets with different widths and depths, and demonstrate the superiorities of the networks by more comparative experiments. We also compare with several recently published deep learning methods in compressive sensing MRI and confirm that our method is advantageous among these deep learning methods.

## 2 RELATED WORK

### 2.1 Model-based CS-MRI Methods

Compressive sensing has shown considerable promise in accelerating the speed of MR acquisition through sparse sampling in  $k$ -space, which has been applied to various MRI applications such as, multi-contrast MRI [21], dynamic MRI [4], [22], etc. Many efforts have been made in model-based CS-MRI method to apply sparse regularization in the gradient domain [23], wavelet transform domain [24], discrete cosine transform domain [3] and contourlet transform domain [25], or patch groups regularized by group sparsity [4], [26]. Although these models are easy and fast to optimize, the usage of a certain sparse transform may introduce staircase artifacts or blocky artifacts in reconstructed images [25]. Combined regularization in some of these transform domains [11] or adaptive transform domain [27] can further improve reconstruction performance. Dictionary learning method relying on a dictionary trained from reference images has also been introduced in CS-MRI model [5], [28], [29]. The non-local method uses groups of similar local patches for joint patch-level reconstruction to better preserve image details [6], [7], [30]. Methods in [8], [31] take the advantages of both the local transforms such as wavelet, TV and nonlocal similarity of the image to improve the reconstruction quality.

In performance, the basic CS-MRI methods with traditional transformation run fast but produce less accurate reconstruction results. Dictionary learning-based and the non-local methods generally output higher quality MR images, but suffer from slow reconstruction speed.

### 2.2 Deep Learning CS-MRI Methods

Deep learning methods are capable of extracting features from data that are useful for recognition and restoration using end-to-end learning. They has been applied to medical imaging to replace the traditional model-based method. The first deep learning method for CS-MRI is in [32]. They trained a deep convolution network for learning the mapping from down-sampled reconstruction images to fully sampled reconstruction images. Method in [33] applies a deep cascade of convolutional neural networks to accelerate MR imaging. Deep residual learning for MR imaging has also been proposed. The work in [34] proposes a single-scale residual learning network and a multi-scale residual learning network (i.e., U-net) for image reconstruction. They show that the U-net which is effective for image segmentation is also valid in estimation of the aliasing artifacts. For deep learning methods, although the reconstruction speed is fast, it is difficult to define the architecture of the network, and training a general deep network requires a large number of training samples.

### 2.3 Discriminative Learning Methods

The discriminative parameter learning approach has been applied to sparse coding [35], Markov Random Filed (MRF) [36], [37], [38] and non-negative matrix factorization [38]. This category of approach links the conventional model-based approaches to the deep learning approaches. The work in [35] implements a truncated form of coordinate

descent algorithm [39] and ISTA algorithm [40] to approximate the estimates of the sparse coding method. Chen et al. [41] and Hammernik et al. [42] learn conventional nonlinear reaction diffusion models with parameterized linear filters and parameterized influence functions to image denoising and reconstruction. Xin et al. [43] unfold the hard thresholding method for a  $l_0$  penalized least square model to a deep neural network. They also explore the network performance of non-shared layers and shared layers. The approaches in [36], [37] learn the optimal shrinkage operators in Markov Random Field model for effective image restoration.

In this paper, we design the ADMM-Net inspired by the ADMM algorithm optimizing a general compressive sensing model for MRI. Compared with the traditional CS-MRI methods, our approach learns optimal parameters, i.e. the parameters in the CS-MRI model and the ADMM algorithm, embedded in a deep architecture. Compared with the widely used deep neural networks, our proposed deep architectures are non-conventional in both structures and operations in network layers. Extensive experiments show that it significantly outperforms the traditional CS-MRI models and widely utilized CNN structures in performance for MR image reconstruction. The ADMM-Net can also be potentially applied to other related problems solving an energy minimization problem using the ADMM algorithm.

### 3 ADMM-NET FOR CS-MRI

In this section, we first introduce a general CS-MRI model and corresponding ADMM iterative procedures. Then, we define a data flow graph derived from the ADMM iterations. Finally, we generalize this data flow graph to construct our deep ADMM-Nets.

#### 3.1 General CS-MRI Model and ADMM Algorithm

As a starting point, we consider reconstructing an MR image by a general compressive sensing MRI (CS-MRI) model.

**General CS-MRI Model:** Assume  $x \in \mathbb{C}^N$  is an MRI image to be reconstructed,  $y \in \mathbb{C}^{N'}$  ( $N' < N$ ) is the under-sampled  $k$ -space data. According to the CS theory, the reconstructed image can be estimated by solving the following optimization problem:

$$\hat{x} = \arg \min_x \left\{ \frac{1}{2} \|Ax - y\|_2^2 + \sum_{l=1}^L \lambda_l g(D_l x) \right\}, \quad (1)$$

where  $A = PF \in \mathbb{R}^{N' \times N}$  is a measurement matrix,  $P \in \mathbb{R}^{N' \times N}$  is an under-sampling matrix,  $F$  is a Fourier transform.  $D_l$  denotes a transform matrix for a filtering operation, e.g., Discrete Wavelet Transform (DWT), Discrete Cosine Transform (DCT), etc.,  $g(\cdot)$  is a regularization function derived from the data prior, e.g.,  $l_q$ -regularizer ( $q \in [0, 1]$ ) for a sparse prior.  $\lambda_l$  is regularization parameter.

The above optimization problem can be solved efficiently by ADMM algorithm. The following solvers are two forms of ADMM algorithm depending on the different auxiliary variables.

**ADMM solver I:** By introducing independent auxiliary variables  $z = \{z_1, z_2, \dots, z_L\}$  in the transform domains, Eqn. (1) is equivalent to:

$$\min_x \frac{1}{2} \|Ax - y\|_2^2 + \sum_{l=1}^L \lambda_l g(z_l) \quad (2)$$

$$s.t. \quad z_l = D_l x, \quad \forall l \in \{1, 2, \dots, L\}.$$

Its augmented Lagrangian function is:

$$\mathcal{L}_\rho(x, z, \alpha) = \frac{1}{2} \|Ax - y\|_2^2 + \sum_{l=1}^L [\lambda_l g(z_l) + \langle \alpha_l, D_l x - z_l \rangle + \frac{\rho_l}{2} \|D_l x - z_l\|_2^2], \quad (3)$$

where  $\alpha = \{\alpha_l\}$  are Lagrangian multipliers representing dual variables and  $\rho = \{\rho_l\}$  are penalty parameters. For simplicity, we use scaled definition of  $\beta_l = \frac{\alpha_l}{\rho_l}$  ( $l \in \{1, 2, \dots, L\}$ ), in this case, ADMM alternatively optimizes  $\{x, z, \beta\}$  by solving the following three subproblems:

$$\left\{ \begin{array}{l} \arg \min_x \frac{1}{2} \|Ax - y\|_2^2 + \sum_{l=1}^L \frac{\rho_l}{2} \|D_l x + \beta_l - z_l\|_2^2, \\ \arg \min_z \sum_{l=1}^L [\lambda_l g(z_l) + \frac{\rho_l}{2} \|D_l x + \beta_l - z_l\|_2^2], \\ \arg \max_\beta \sum_{l=1}^L \langle \beta_l, D_l x - z_l \rangle. \end{array} \right. \quad (4)$$

Substitute  $A = PF$  into Eqn. (4), then the three subproblems have the following solutions:

$$\left\{ \begin{array}{l} \mathbf{X}^{(n)} : x^{(n)} = F^T [P^T P + \sum_{l=1}^L \rho_l F D_l^T D_l F^T]^{-1} \\ \quad [P^T y + \sum_{l=1}^L \rho_l F D_l^T (z_l^{(n-1)} - \beta_l^{(n-1)})], \\ \mathbf{Z}^{(n)} : z_l^{(n)} = \mathcal{S}(D_l x^{(n)} + \beta_l^{(n-1)}; \lambda_l / \rho_l), \\ \mathbf{M}^{(n)} : \beta_l^{(n)} = \beta_l^{(n-1)} + \eta_l (D_l x^{(n)} - z_l^{(n)}), \end{array} \right. \quad (5)$$

where  $n \in \{1, 2, \dots, N_s\}$  denotes  $n$ -th iteration and the superscript  $T$  refers to the transpose and conjugate transpose operator for real and complex data respectively. Operation  $x^{(n)}$  can be efficiently computed by fast Fourier transform (FFT) because  $P^T P + \sum_{l=1}^L \rho_l F D_l^T D_l F^T$  is diagonal matrix.  $\mathcal{S}(\cdot)$  is a nonlinear shrinkage function with the parameters  $\lambda_l / \rho_l$ ,  $l \in \{1, 2, \dots, L\}$ . It is usually a soft or hard thresholding function corresponding to the sparse regularization of  $l_1$  and  $l_0$  regularizer respectively [44]. The parameter  $\eta_l$  is an update rate for updating the multiplier.

**ADMM solver II:** By introducing the auxiliary variable  $z$  in the spatial domain (i.e., image domain), Eqn. (1) is equivalent to:

$$\min_{x, z} \frac{1}{2} \|Ax - y\|_2^2 + \sum_{l=1}^L \lambda_l g(D_l z) \quad (6)$$

$$s.t. \quad z = x.$$

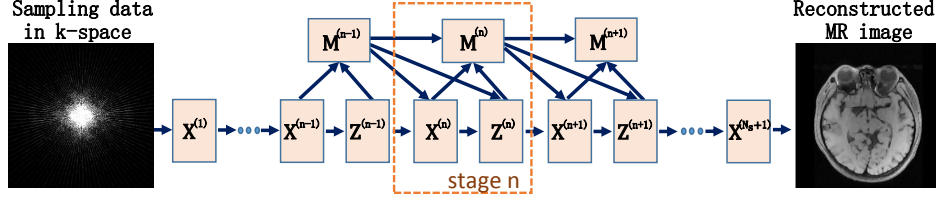


Fig. 1. The data flow graph for the ADMM optimization of a general CS-MRI model. This graph consists of three types of nodes: reconstruction ( $\mathbf{X}$ ), denoising ( $\mathbf{Z}$ ), and multiplier update ( $\mathbf{M}$ ). An under-sampled data in  $k$ -space is successively processed over the graph, and finally generates an MR image. Our deep ADMM-Nets are defined over this data flow graph.

In this way, its augmented Lagrangian function is :

$$\mathcal{L}_\rho(x, z, \alpha) = \frac{1}{2} \|Ax - y\|_2^2 + \sum_{l=1}^L \lambda_l g(D_l z) + \langle \alpha, x - z \rangle + \frac{\rho}{2} \|x - z\|_2^2. \quad (7)$$

Using the scaled Lagrangian multiplier  $\beta = \frac{\alpha}{\rho}$ , we can express the subproblems as:

$$\begin{cases} \arg \min_x \frac{1}{2} \|Ax - y\|_2^2 - \frac{\rho}{2} \|x + \beta - z\|_2^2, \\ \arg \min_z \sum_{l=1}^L \lambda_l g(D_l z) + \frac{\rho}{2} \|x + \beta - z\|_2^2, \\ \arg \max_\beta \langle \beta, x - z \rangle. \end{cases} \quad (8)$$

One way to solve the second subproblem is to directly employ gradient-descent algorithm, which yields the ADMM algorithm iterations:

$$\begin{cases} \mathbf{X}^{(n)} : x^{(n)} = F^T (P^T P + \rho I)^{-1} \\ \quad [P^T y + \rho F(z^{(n-1)} - \beta^{(n-1)})], \\ \mathbf{Z}^{(n)} : z^{(n,k)} = \mu_1 z^{(n,k-1)} + \mu_2 (x^{(n)} + \beta^{(n-1)}) \\ \quad - \sum_{l=1}^L \tilde{\lambda}_l D_l^T \mathcal{H}(D_l z^{(n,k-1)}), \\ \mathbf{M}^{(n)} : \beta^{(n)} = \beta^{(n-1)} + \tilde{\eta} (x^{(n)} - z^{(n)}), \end{cases} \quad (9)$$

where  $I$  is an unit matrix with size of  $N \times N$ .  $\mu_1 = 1 - l_r \rho$ ,  $\mu_2 = l_r \rho$ ,  $\tilde{\lambda}_l = l_r \lambda_l$ ,  $l_r$  is the step size and  $k \in \{1, 2, \dots, N_k\}$  denotes the number of iterations in the gradient-descent method, therefore  $z^{(n)} = z^{(n, N_k)}$ .  $\mathcal{H}(\cdot)$  refers to a nonlinear transform corresponding to the gradient of regularization function  $g(\cdot)$ . The parameter  $\tilde{\eta}$  is an update rate as well.

In CS-MRI, it commonly needs to run the ADMM algorithm in dozens of iterations to get a satisfactory reconstruction result. However, it is challenging to choose the appropriate transform  $D_l$ , and nonlinear function  $\mathcal{S}(\cdot)$  or  $\mathcal{H}(\cdot)$  for general regularization function  $g(\cdot)$ . Moreover, it is also non-trivial to tune the parameters  $\rho_l$ ,  $\eta_l$ ,  $\mu_1$ ,  $\mu_2$ ,  $\tilde{\lambda}_l$ , etc., in ADMM solvers for reconstructing  $k$ -space data with different sampling rates. To overcome these difficulties, we will design a data flow graph for the ADMM algorithm, over which we can define deep ADMM-Nets to discriminatively learn all the above transforms, functions, and parameters.

### 3.2 Data Flow Graph for ADMM Algorithm

To design our deep ADMM-Net, we first map both ADMM iterative procedures in Eqn. (5) and Eqn. (9) to one data flow

graph. As shown in Fig. 1, this graph comprises of *nodes* corresponding to different operations in ADMM algorithm, and *directed edges* corresponding to the data flows between operations. In this case, the  $n$ -th iteration of ADMM algorithm corresponds to the  $n$ -th stage of the data flow graph. In each stage of the graph, there are three types of nodes mapped from three types of operations in ADMM, i.e., reconstruction operation ( $\mathbf{X}$ ) for restoring an image from Fourier transform domain, denoising operation ( $\mathbf{Z}$ ) regarded as denoising the image  $D_l x + \beta_l$ ,  $l \in \{1, 2, \dots, L\}$  in Eqn. (4) or  $x + \beta$  in Eqn. (8), and multiplier update operation ( $\mathbf{M}$ ). The whole data flow graph is a multiple repetition of the above stages corresponding to successive iterations in ADMM. Given an under-sampled data in  $k$ -space, it flows over the graph and finally generates a reconstructed image. In this way, we map the ADMM iterations to a data flow graph, which is useful to define and train our deep ADMM-Nets in the following.

### 3.3 Deep ADMM-Nets

Our deep ADMM-Nets are defined over the data flow graph. They keep the graph structure but generalize and decompose the three types of operations to have learnable parameters as network layers. These operations are now generalized as reconstruction layer, convolution layer, non-linear transform layer, multiplier update layer, and so on. We next discuss them in details.

#### 3.3.1 Basic-ADMM-Net

Based on the iterative algorithm in ADMM solver I, i.e., Eqn. (5), we define a deep network called Basic-ADMM-Net shown in Fig. 2. It generalizes the reconstruction operation  $\mathbf{X}^{(n)}$  to reconstruction layer, decomposes the denoising operation  $\mathbf{Z}^{(n)}$  to convolution layer derive from the operation  $\{D_l x^{(n)}\}_{l=1}^L$  and non-linear transform layer, finally extends the multiplier update procedure  $\mathbf{M}^{(n)}$  in Eqn. (5) to multiplier update layer.

**Reconstruction layer ( $\mathbf{X}^{(n)}$ ):** This layer reconstructs an MRI image following the reconstruction operation  $\mathbf{X}^{(n)}$  in Eqn. (5). Given the inputs  $z_l^{(n-1)}$  and  $\beta_l^{(n-1)}$ , the output of this layer is defined as:

$$x^{(n)} = F^T (P^T P + \sum_{l=1}^L \rho_l^{(n)} F H_l^{(n)T} H_l^{(n)} F^T)^{-1} [P^T y + \sum_{l=1}^L \rho_l^{(n)} F H_l^{(n)T} (z_l^{(n-1)} - \beta_l^{(n-1)})], \quad (10)$$

where  $H_l^{(n)}$  is the  $l$ -th filter with size of  $w_f \times w_f$  in stage  $n$ ,  $\rho_l^{(n)}$  is the  $l$ -th penalty parameter,  $l = 1, \dots, L$ , and  $y$  is

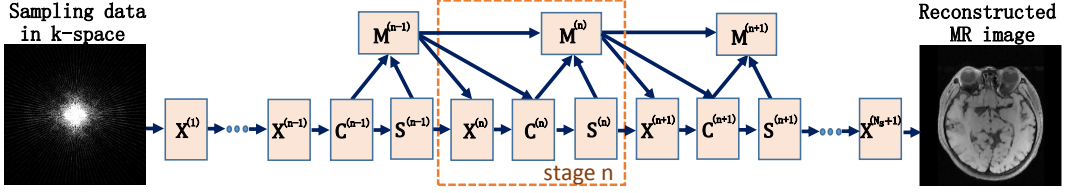


Fig. 2. The architecture of a deep Basic-ADMM-Net. There are four layers including reconstruction layer ( $\mathbf{X}^{(n)}$ ), convolution layer ( $\mathbf{C}^{(n)}$ ), nonlinear transform layer ( $\mathbf{S}^{(n)}$ ) and multiplier update layer ( $\mathbf{M}^{(n)}$ ) in each stage.

the input under-sampled data in  $k$ -space. In the first stage (i.e.,  $n = 1$ ),  $z_l^{(0)}$  and  $\beta_l^{(0)}$  are initialized to zeros, therefore  $x^{(1)} = F^T(P^T P + \sum_{l=1}^L \rho_l^{(1)} F H_l^{(1)T} H_l^{(1)} F^T)^{-1}(P^T y)$ .

**Convolution layer ( $\mathbf{C}^{(n)}$ ):** It performs convolution operation to transform an image into transform domain. To represent images, a traditional choice is using a set of pre-trained bases such as DCT, Fourier, Haar, etc. In our formulation, we represent the image by a set of learnable filters equivalently. Given an image  $x^{(n)}$ , i.e., a reconstructed image in  $n$ -th stage, the output is

$$c_l^{(n)} = D_l^{(n)} x^{(n)}, \quad (11)$$

where  $D_l^{(n)}$  is a matrix corresponding to the  $l$ -th filter with size of  $w_f \times w_f$  in stage  $n$ . Different from the original ADMM, we do not constrain the filters  $H_l^{(n)}$  and  $D_l^{(n)}$  to be the same to increase the network capacity.

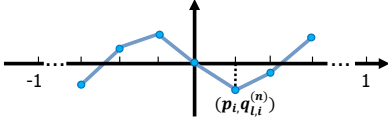


Fig. 3. Illustration of a piecewise linear function determined by a set of control points  $(p_i, q_{l,i}^{(n)})$ .

**Nonlinear transform layer ( $\mathbf{S}^{(n)}$ ):** This layer performs nonlinear transform inspired by the shrinkage function  $\mathcal{S}(\cdot)$  defined in  $\mathbf{Z}^{(n)}$  from Eqn. (5). Instead of setting it to be a shrinkage function determined by the regularization term  $g(\cdot)$  in Eqn. (1), we aim to learn more general function using piecewise linear function. Given  $c_l^{(n)}$  and  $\beta_l^{(n-1)}$ , the output of this layer is defined as:

$$z_l^{(n)} = S_{PLF}(c_l^{(n)} + \beta_l^{(n-1)}; \{p_i, q_{l,i}^{(n)}\}_{i=1}^{N_c}), \quad (12)$$

where  $S_{PLF}(\cdot)$  is a piecewise linear function determined by a set of control points  $\{p_i, q_{l,i}^{(n)}\}_{i=1}^{N_c}$ . i.e.,

$$S_{PLF}(a) = \begin{cases} a + q_{l,1}^{(n)} - p_1, & a < p_1, \\ a + q_{l,N_c}^{(n)} - p_{N_c}, & a > p_{N_c}, \\ q_{l,r}^{(n)} + \frac{(a-p_r)(q_{l,r+1}^{(n)} - q_{l,r}^{(n)})}{p_{r+1} - p_r}, & p_1 \leq a \leq p_{N_c}, \end{cases}$$

where  $r = \lfloor \frac{a-p_1}{p_2-p_1} \rfloor$ ,  $\{p_i\}_{i=1}^{N_c}$  are predefined positions uniformly located within  $[-1,1]$ , and  $\{q_{l,i}^{(n)}\}_{i=1}^{N_c}$  are the values at these positions for  $l$ -th filter in  $n$ -th stage. Figure 3 gives an illustrative example. Since a piecewise linear function can approximate any function, we can learn flexible nonlinear

transform function from data beyond the off-the-shelf hard or soft thresholding functions.

**Multiplier update layer ( $\mathbf{M}^{(n)}$ ):** Given three inputs  $\beta_l^{(n-1)}$ ,  $c_l^{(n)}$  and  $z_l^{(n)}$ , the output of this layer is defined as:

$$\beta_l^{(n)} = \beta_l^{(n-1)} + \eta_l^{(n)}(c_l^{(n)} - z_l^{(n)}), \quad (13)$$

where  $\eta_l^{(n)}$  is a learnable parameter.

**Network Parameters:** In this deep architecture, we aim to learn the following parameters:  $H_l^{(n)}$  and  $\rho_l^{(n)}$  in reconstruction layer, filter  $D_l^{(n)}$  in convolution layer, the values  $\{q_{l,i}^{(n)}\}_{i=1}^{N_c}$  in nonlinear transform layer, and  $\eta_l^{(n)}$  in multiplier update layer, where  $l \in \{1, 2, \dots, L\}$  and  $n \in \{1, 2, \dots, N_s\}$  are the indexes for the filters and stages respectively. All of these parameters are taken as the network parameters to be learned.

Figure 4 shows an example of a deep Basic-ADMM-Net with three stages. The under-sampled data in  $k$ -space flows over three stages in a order from circled number 1 to number 12, followed by a final reconstruction layer with circled number 13 and generates a reconstructed MR image. Immediate reconstruction result at each stage is shown under each reconstruction layer.

### 3.3.2 Generic-ADMM-Net

From the iterative operations in ADMM solver II, i.e., Eqn. (9), we extend the data flow graph to a deep Generic-ADMM-Net as shown in Fig. 5. Each stage of the network corresponds to one iteration of the ADMM algorithm in Eqn. (9), and each sub-stage of the network corresponds to iterations of the gradient-descent algorithm implementing  $\mathbf{Z}^{(n)}$  in Eqn. (9). Compared with the Basic-ADMM-Net, the Generic-ADMM-Net has a different reconstruction layer  $\mathbf{X}^{(n)}$  and a generalized denoising layer  $\mathbf{Z}^{(n)}$  in each stage.

**Reconstruction layer ( $\mathbf{X}^{(n)}$ ):** Given  $z^{(n-1)}$  and  $\beta^{(n-1)}$ , the output of this layer is defined as:

$$x^{(n)} = F^T(P^T P + \rho^{(n)} I)^{-1} [P^T y + \rho^{(n)} F(z^{(n-1)} - \beta^{(n-1)})], \quad (14)$$

where  $\rho^{(n)}$  is a learnable penalty parameter and  $y$  is the input under-sampled data in  $k$ -space. In the first stage (i.e.,  $n = 1$ ),  $z_l^{(0)}$  and  $\beta_l^{(0)}$  are also initialized to zeros, therefore  $x^{(1)} = F^T(P^T P + \rho^{(1)} I)^{-1}(P^T y)$ .

We next introduce the denoising layer  $\mathbf{Z}^{(n)}$ . We decompose  $\mathbf{Z}^{(n)}$  in Eqn. (9) to several sub-layers, such as addition layer, convolution layer and non-linear transform layer. The iterative stacking of these sub-layers just implement the iterative gradient descent in  $\mathbf{Z}^{(n)}$  of Eqn. (9). For the  $k$ -th

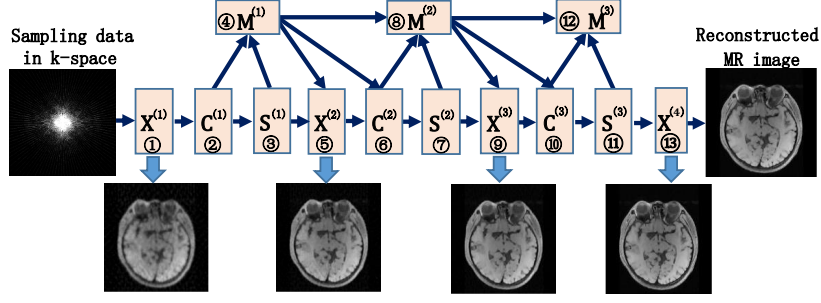


Fig. 4. An example of a deep Basic-ADMM-Net with three stages. The sampled data in  $k$ -space is successively processed by operations in a order from 1 to 12, followed by a reconstruction layer  $X^{(4)}$  to output the final reconstructed image. The reconstructed image in each stage is shown under each reconstruction layer.

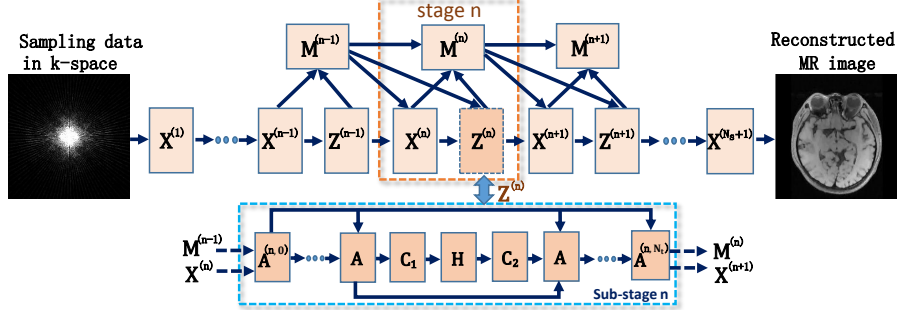


Fig. 5. The architecture of a deep Generic-ADMM-Net. There are three layers including reconstruction layer ( $X^{(n)}$ ), denoising layer ( $Z^{(n)}$ ) and multiplier update layer ( $M^{(n)}$ ) in each stage. The denoising layer  $Z^{(n)}$  is decomposed to  $N_t$  iterations consisting of addition layer (A), convolution layers ( $C_1$ ,  $C_2$ ) and non-linear transform layer (H) in each sub-stage.

iteration ( $k \in \{1, 2, \dots, N_t\}$ ) in the  $n$ -th sub-stage in Fig. 5, these sub-layers are defined as follows.

**Addition layer ( $A^{(n,k)}$ ):** It performs simple weighted summation operation. Given  $x^{(n)}$ ,  $\beta^{(n-1)}$ ,  $z^{(n,k-1)}$  and  $c_2^{(n,k)}$ , the output of this layer is

$$z^{(n,k)} = \mu_1^{(n,k)} z^{(n,k-1)} + \mu_2^{(n,k)} (x^{(n)} + \beta^{(n-1)}) - c_2^{(n,k)}, \quad (15)$$

where  $\mu_1^{(n,k)}$  and  $\mu_2^{(n,k)}$  are weighting parameters.  $z^{(n,0)}$  is initialized to  $x^{(n)} + \beta^{(n-1)}$ , therefore  $z^{(n,1)} = x^{(n)} + \beta^{(n-1)} - c_2^{(n,1)}$  due to  $\mu_1 + \mu_2 = 1$  in Eqn. (9). The output of the  $n$ -th sub-stage is  $z^{(n)} = z^{(n,N_t)}$ .

**Convolution layer ( $C_1^{(n,k)}$ ,  $C_2^{(n,k)}$ ):** Given the input  $z^{(n,k-1)}$  and  $h^{(n,k)}$ , we define two convolution layers as:

$$c_1^{(n,k)} = w_1^{(n,k)} * z^{(n,k-1)} + b_1^{(n,k)}, \quad (16)$$

$$c_2^{(n,k)} = w_2^{(n,k)} * h^{(n,k)} + b_2^{(n,k)}, \quad (17)$$

where  $w_1^{(n,k)}$  corresponds to  $L$  filters with size of  $w_f \times w_f$ ,  $b_1^{(n,k)}$  is an  $L$ -dimensional biases vector,  $w_2^{(n,k)}$  corresponds to a filter with size of  $f \times f \times L$ , and  $b_2^{(n,k)}$  is a 1-dimensional biases vector. We integrate feature extraction and feature fusion in the second convolution operation, the output  $c_1^{(n,k)}$  is composed of  $L$  feature maps and the output  $c_2^{(n,k)}$  is a feature map which has the same size as the image to be reconstructed, therefore we generalize the operation  $\sum_{l=1}^L \lambda_l D_l^T \mathcal{H}(D_l z^{(n,k-1)})$  of Eqn. (9) to the operation  $w_2^{(n,k)} * \mathcal{H}(w_1^{(n,k)} * z^{(n,k-1)} + b_1^{(n,k)}) + b_2^{(n,k)} = c_2^{(n,k)}$ .

**Nonlinear transform layer ( $H^{(n,k)}$ ):** We still learn more general function using piecewise linear function for  $\mathcal{H}(\cdot)$  defined in  $Z^{(n)}$  in Eqn. (9). Given the input  $c_1^{(n,k)}$ , the

output of this layer is defined as:

$$h^{(n,k)} = S_{PLF}(c_1^{(n,k)}; \{p_i, q_i^{(n,k)}\}_{i=1}^{N_c}), \quad (18)$$

where  $\{p_i\}_{i=1}^{N_c}$  are predefined positions uniformly located within  $[-1, 1]$ , and  $\{q_i^{(n,k)}\}_{i=1}^{N_c}$  are the values at these positions for  $k$ -th iteration in the sub-stage  $n$ .

Generic-ADMM-Net also generalizes the multiplier update procedure  $M^{(n)}$  in Eqn. (9) to multiplier update layer.

**Multiplier update layer ( $M^{(n)}$ ):** The output of this layer in stage  $n$  is defined as:

$$\beta^{(n)} = \beta^{(n-1)} + \tilde{\eta}^{(n)}(x^{(n)} - z^{(n)}), \quad (19)$$

where  $\tilde{\eta}^{(n)}$  is a learnable parameter in  $n$ -th stage.

**Network Parameters:** In this deep architecture, we aim to learn the following parameters:  $\rho^{(n)}$  in reconstruction layer,  $\mu_1^{(n,k)}$  and  $\mu_2^{(n,k)}$  in addition layer, filters  $w_1^{(n,k)}$ ,  $w_2^{(n,k)}$ , biases  $b_1^{(n,k)}$ ,  $b_2^{(n,k)}$  in convolution layers,  $\{q_i^{(n,k)}\}_{i=1}^{N_c}$  in nonlinear transform layer and  $\tilde{\eta}^{(n)}$  in multiplier update layer, where  $n \in \{1, 2, \dots, N_s\}$  and  $k \in \{1, 2, \dots, N_t\}$  index the stages and the iterations in a sub-stage respectively. Figure 6 shows an example of a Generic-ADMM-Net with three stages and one iteration in each sub-stage.

### 3.3.3 Complex-ADMM-Net

Generally, MR images are complex-valued images, and their phase information is also important for medical applications. Unlike many other popular deep networks designed for applications processing real-valued data, we generalize our Generic-ADMM-Net to reconstruct complex-valued MR images, dubbed Complex-ADMM-Net. Compared with

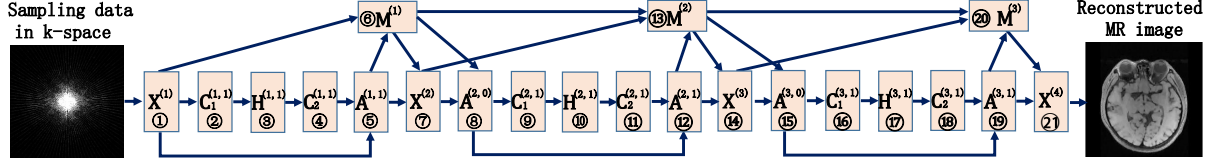


Fig. 6. An example of deep Generic-ADMM-Net with three stages and one iteration in each sub-stage ( $n = 3, N_i = 1$ ). The sampled data in  $k$ -space is successively processed by operations in an order from 1 to 20, followed by a reconstruction layer  $X^{(4)}$  to output the final reconstructed image.

Generic-ADMM-Net, the Complex-ADMM-Net has a generalized operation in the nonlinear transform layer.

For the convolution layers, we still use real-valued filters to convolve complex-valued data. It means that the filters in convolution layers are all real-valued, and the convolution is performed between the real-valued filters and complex-valued inputs. This is equivalently to performing convolution over real and imagery parts of layer input separately using shared real-valued filters.

For the nonlinear transform layer, we deal with real and imaginary parts separately, i.e.,

$$h^{(n,k)} = S_{PLF}(\mathbf{Re}(c_1^{(n,k)})) + jS_{PLF}(\mathbf{Im}(c_1^{(n,k)})), \quad (20)$$

where  $\mathbf{Re}(\cdot)$  is an operator for the real part and  $\mathbf{Im}(\cdot)$  is an operator for the imaginary part. Both the real and imagery parts share the same piecewise linear transform function.

## 4 NETWORK TRAINING

We take the reconstructed MR image from fully sampled data in  $k$ -space as the ground-truth MR image  $x^{gt}$ , and under-sampled data  $y$  in  $k$ -space as the input. Then a training set  $\Gamma$  is constructed containing pairs of under-sampled data and ground-truth MR image. We choose normalized mean square error (NMSE) as the loss function in network training. Given pairs of training data, the loss between the network output and the ground-truth is defined as:

$$E(\Theta) = \frac{1}{|\Gamma|} \sum_{(y, x^{gt}) \in \Gamma} \frac{\|\hat{x}(y, \Theta) - x^{gt}\|_2}{\|x^{gt}\|_2}, \quad (21)$$

where  $\hat{x}(y, \Theta)$  is the network output based on network parameter  $\Theta$  and under-sampled data  $y$  in  $k$ -space. The NMSE is a widely-used evaluation criteria for image reconstruction, and ADMM-Nets also permit usage of other kinds of evaluation metrics such as SSIM, PSNR, SNR, etc. We learn the parameters  $\Theta = \{H_l^{(n)}, \rho_l^{(n)}, D_l^{(n)}, \{q_{l,i}^{(n)}\}_{i=1}^{N_c}, \eta_l^{(n)}\}_{n=1}^{N_s} \cup \{H_l^{(N_s+1)}, \rho_l^{(N_s+1)}\}$  ( $l=1, \dots, L$ ) for Basic-ADMM-Net, and parameters  $\Theta = \{\rho^{(n)}, \mu_1^{(n,k)}, \mu_2^{(n,k)}, w_1^{(n,k)}, b_1^{(n,k)}, w_2^{(n,k)}, b_2^{(n,k)}, \{q_i^{(n,k)}\}_{i=1}^{N_c}, \tilde{\eta}^{(n)}\}_{n=1}^{N_s} \cup \{\rho^{(N_s+1)}\}$  in Generic-ADMM-Net by minimizing the loss w.r.t. these parameters using gradient-based algorithm L-BFGS<sup>1</sup>. In the following, we first discuss the initialization of parameters and then compute the gradients of the loss  $E(\Theta)$  w.r.t. parameters  $\Theta$  using back-propagation (BP) over the networks.

### 4.1 Initialization

We initialize the network parameters by model-based initialization method and random initialization method.

1. <http://users.eecs.northwestern.edu/~nocedal/lbfgsb.html>

**Model-based initialization:** We initialize parameters  $\Theta$  in the ADMM-Nets according to the ADMM solvers of the following baseline CS-MRI model

$$\arg \min_x \left\{ \frac{1}{2} \|Ax - y\|_2^2 + \lambda \sum_{l=1}^L \|D_l x\|_1 \right\}. \quad (22)$$

In this model, we set  $D_l$  as a DCT basis and impose  $l_1$ -norm regularizer in the DCT transform space. Then, the function  $S(\cdot)$  in ADMM algorithm (Eqn. (5)) is a soft thresholding function:  $S(a; \lambda/\rho_l) = \text{sgn}(a)(|a| - \lambda/\rho_l)$  when  $|a| > \lambda/\rho_l$ , and 0 otherwise. For each  $n$ -th stage of the networks, filters  $D_l^{(n)}$ ,  $w_l^{(n)}$ ,  $w_1^{(n,k)}$  and  $w_2^{(n,k)}$  are initialized to be  $D_l$  ( $l = 1, \dots, L$ ) from Eqn. (22). For the nonlinear transform layers, we uniformly choose 101 positions located within  $[-1,1]$ , each value  $q_{l,i}^{(n)}$  is initialized as  $S(p_i; \lambda/\rho_l)$ . Other parameters are initialized to be the corresponding values in the ADMM algorithm. In this case, the initialized net is exactly a realization of ADMM optimizing process, and the optimization of the network parameters is expected to produce improved reconstruction result.

**Random initialization:** In the deep learning literatures, the weights in deep networks are generally initialized by random values. In such initialization, for  $n$ -th stage of the ADMM-Nets, filters are initialized by values randomly sampled from a Gaussian distribution with zero mean and well chosen variance level [45]. Each value of the predefined positions (i.e.,  $q_i^{(n)}$ ) in a non-linear transform layer is initialized as  $\text{max}(p_i, 0)$  implementing a rectified linear unit (ReLU) function.

### 4.2 Gradient Computation by Back-propagation

We compute the gradients of loss w.r.t. parameters using back-propagation over the deep architecture in Fig. 1. In the forward pass, we process the data of  $n$ -th stage in the order of  $\mathbf{X}^{(n)}$ ,  $\mathbf{Z}^{(n)}$ ,  $\mathbf{M}^{(n)}$ . In the backward pass, the gradients are computed in an inverse order. Figures 4 and 6 show the examples, where the gradients can be computed backwardly from the layers with circled number 13 (or 21) to 1 successively. For  $n$ -th stage in Generic-ADMM-Net, Fig. 7 shows five types of nodes (i.e., network layers) and the data flow over them. Each node has multiple inputs and (or) outputs. We next briefly introduce the gradients computation for each layer in a typical stage  $n$  of Generic-ADMM-Net. The method of gradient computation in the Basic-ADMM-Net is similar as Generic-ADMM-Net. Please refer to supplementary material for more details.

**Multiplier update layer ( $\mathbf{M}^{(n)}$ ):** As shown in Fig. 7(a), this layer has three inputs:  $\beta^{(n-1)}$ ,  $x^{(n)}$  and  $z^{(n)}$ . Its output  $\beta^{(n)}$  is the input to compute  $\beta^{(n+1)}$ ,  $z^{(n+1)}$  and  $x^{(n+1)}$ . The

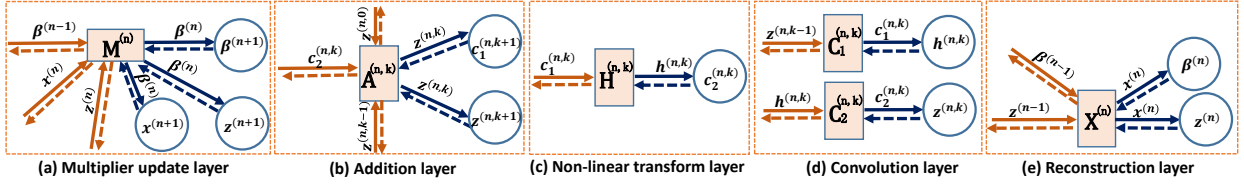


Fig. 7. Illustration of five types of graph nodes (i.e., layers in network) and their data flows in stage  $n$ . The solid arrow indicates the data flow in forward pass and dashed arrow indicates the backward pass when computing gradients in back-propagation.

parameter of this layer is  $\tilde{\eta}^{(n)}$ . The gradient of loss w.r.t. the parameter can be computed as:

$$\frac{\partial E}{\partial \tilde{\eta}^{(n)}} = \frac{\partial E}{\partial \beta^{(n)T}} \frac{\partial \beta^{(n)}}{\partial \tilde{\eta}^{(n)}} = \frac{\partial E}{\partial \beta^{(n)T}} (x^{(n)} - z^{(n)}),$$

where  $\frac{\partial E}{\partial \beta^{(n)T}} = \frac{\partial E}{\partial \beta^{(n+1)T}} \frac{\partial \beta^{(n+1)}}{\partial \beta^{(n)}} + \frac{\partial E}{\partial z^{(n+1)T}} \frac{\partial z^{(n+1)}}{\partial \beta^{(n)}} + \frac{\partial E}{\partial x^{(n+1)T}} \frac{\partial x^{(n+1)}}{\partial \beta^{(n)}}$ , is the summation of gradients along three dashed blue arrows in Fig. 7(a). We also compute gradients of the loss w.r.t. its inputs in this layer for gradient propagation:

$$\begin{aligned} \frac{\partial E}{\partial \beta^{(n-1)}} &= \frac{\partial E}{\partial \beta^{(n)T}} \frac{\partial \beta^{(n)}}{\partial \beta^{(n-1)}} = \frac{\partial E}{\partial \beta^{(n)T}}, \\ \frac{\partial E}{\partial x^{(n)}} &= \tilde{\eta}^{(n)} \frac{\partial E}{\partial \beta^{(n)T}}, \quad \frac{\partial E}{\partial z^{(n)}} = -\frac{\partial E}{\partial x^{(n)}}. \end{aligned}$$

**Addition layer ( $A^{(n,k)}$ ):** The parameters of this layer are  $\mu_1^{(n,k)}$  and  $\mu_2^{(n,k)}$ . As shown in Fig. 7(b), the output  $z^{(n,k)}$  is the input for computing  $c_1^{(n,k+1)}$  and  $z^{(n,k+1)}$  in the next layers. The gradients of loss w.r.t. parameters can be computed as

$$\frac{\partial E}{\partial \mu_1^{(n,k)}} = \frac{\partial E}{\partial z^{(n,k)T}} z^{(n,k-1)}, \quad \frac{\partial E}{\partial \mu_2^{(n,k)}} = \frac{\partial E}{\partial z^{(n,k)T}},$$

where  $\frac{\partial E}{\partial z^{(n,k)T}} = \frac{\partial E}{\partial c_1^{(n,k+1)T}} \frac{\partial c_1^{(n,k+1)}}{\partial z^{(n,k)}} + \frac{\partial E}{\partial z^{(n,k+1)T}} \frac{\partial z^{(n,k+1)}}{\partial z^{(n,k)}}$ . The gradients of the loss w.r.t. the inputs in this layer are:

$$\begin{aligned} \frac{\partial E}{\partial z^{(n,k-1)}} &= \mu_1^{(n,k)} \frac{\partial E}{\partial z^{(n,k)T}}, \quad \frac{\partial E}{\partial c_2^{(n,k)}} = -\frac{\partial E}{\partial z^{(n,k)T}}, \\ \frac{\partial E}{\partial x^{(n)}} &= \frac{\partial E}{\partial \beta^{(n-1)}} = \mu_2^{(n,k)} \frac{\partial E}{\partial z^{(n,k)T}}. \end{aligned}$$

**Nonlinear transform layer ( $H^{(n,k)}$ ):** As shown in Fig. 7(c), this layer has one input:  $c_1^{(n,k)}$ , and its output  $h^{(n,k)}$  is the input for computing  $c_2^{(n,k)}$ . The parameters of this layer are  $\{q_i^{(n,k)}\}_{i=1}^{N_c}$ . The gradient of loss w.r.t. parameters can be computed as

$$\frac{\partial E}{\partial q_i^{(n,k)}} = \frac{\partial E}{\partial h^{(n,k)T}} \frac{\partial h^{(n,k)}}{\partial q_i^{(n,k)}},$$

where  $\frac{\partial E}{\partial h^{(n,k)T}} = \frac{\partial E}{\partial c_2^{(n,k)T}} \frac{\partial c_2^{(n,k)}}{\partial h^{(n,k)}}$ . The calculation of  $\frac{\partial h^{(n,k)}}{\partial q_i^{(n,k)}}$  and  $\frac{\partial h^{(n,k)}}{\partial c_1^{(n,k)}}$  can be found in the supplementary material.

**Convolution layer ( $C_1^{(n,k)}, C_2^{(n,k)}$ ):** As shown in Fig. 7(d), a convolution layer has one input and one output. The parameters of  $C_1^{(n,k)}$  layer and  $C_2^{(n,k)}$  layer are  $w_1^{(n,k)}, b_1^{(n,k)}, w_2^{(n,k)}$  and  $b_2^{(n,k)}$ . The gradient of loss w.r.t.

parameters can be computed as

$$\begin{aligned} \frac{\partial E}{\partial w_1^{(n,k)}} &= \frac{\partial E}{\partial c_1^{(n,k)T}} \frac{\partial c_1^{(n,k)}}{\partial w_1^{(n,k)}}, \quad \frac{\partial E}{\partial b_1^{(n,k)}} = \frac{\partial E}{\partial c_1^{(n,k)T}}, \\ \frac{\partial E}{\partial w_2^{(n,k)}} &= \frac{\partial E}{\partial c_2^{(n,k)T}} \frac{\partial c_2^{(n,k)}}{\partial w_2^{(n,k)}}, \quad \frac{\partial E}{\partial b_2^{(n,k)}} = \frac{\partial E}{\partial c_2^{(n,k)T}}. \end{aligned}$$

Where  $\frac{\partial E}{\partial c_1^{(n,k)T}} = \frac{\partial E}{\partial h^{(n,k)T}} \frac{\partial h^{(n,k)}}{\partial c_1^{(n,k)}}$ ,  $\frac{\partial E}{\partial c_2^{(n,k)T}} = \frac{\partial E}{\partial z^{(n,k)T}} \frac{\partial z^{(n,k)}}{\partial c_2^{(n,k)}}$ . We also compute gradients of the loss w.r.t. its inputs in this layer for back propagation:

$$\frac{\partial E}{\partial z^{(n,k-1)}} = \frac{\partial E}{\partial c_1^{(n,k)T}} \frac{\partial c_1^{(n,k)}}{\partial z^{(n,k-1)}}, \quad \frac{\partial E}{\partial h^{(n,k)}} = \frac{\partial E}{\partial c_2^{(n,k)T}} \frac{\partial c_2^{(n,k)}}{\partial h^{(n,k)}}.$$

**Reconstruction layer ( $X^{(n)}$ ):** The parameter in this layer is  $\rho^{(n)}$  for  $n$ -th stage. The gradient of loss w.r.t. the parameter is computed as

$$\begin{aligned} \frac{\partial E}{\partial \rho^{(n)}} &= \frac{\partial E}{\partial x^{(n)T}} F^T Q \{F(z^{(n-1)} - \beta^{(n-1)}) \\ &\quad - Q[P^T y + \rho^{(n)} F(z^{(n-1)} - \beta^{(n-1)})]\}, \end{aligned}$$

where  $Q = (P^T P + \rho^{(n)} I)^{-1}$ , and  $\frac{\partial E}{\partial x^{(n)T}}$  is

$$\frac{\partial E}{\partial x^{(n)T}} = \begin{cases} \frac{\partial E}{\partial \beta^{(n)T}} \frac{\partial \beta^{(n)}}{\partial x^{(n)}} + \frac{\partial E}{\partial z^{(n)T}} \frac{\partial z^{(n)}}{\partial x^{(n)}}, & n \leq N_s, \\ \frac{1}{|\Gamma|} \frac{(x^{(n)} - x^{g^t})}{\|x^{(n)} - x^{g^t}\|_2}, & n = N_s + 1. \end{cases}$$

The gradient of loss w.r.t. input in this layer is computed as

$$\frac{\partial E}{\partial z^{(n-1)}} = [\rho^{(n)} F^T Q F \frac{\partial E}{\partial x^{(n)}}]^T = -\frac{\partial E}{\partial \beta^{(n-1)}}.$$

**Complex-ADMM-Net:** Compared with the gradient computation in Generic-ADMM-Net, in each layer, the gradients of the parameters are the sum of the gradients from the real and imaginary parts of the outputs. In the Complex-ADMM-Net, the gradients of loss w.r.t. parameters can be calculated by the following formulations:

$$\frac{\partial E}{\partial \Theta} = \{\text{Re}(\frac{\partial E}{\partial O_t}) \text{Re}(\frac{\partial O_t}{\partial \Theta_t}) + \text{Im}(\frac{\partial E}{\partial O_t}) \text{Im}(\frac{\partial O_t}{\partial \Theta_t})\}_{t=1}^{N_l},$$

where  $N_l$  is the number of net layers,  $O_t$  is the output of the  $t$ -th layer, and  $\Theta_t$  represents the parameters in this layer.

## 5 EXPERIMENTS

In this section, we conduct extensive experimental evaluations for the proposed ADMM-Nets. We train and test ADMM-Nets on brain and chest MR images<sup>2</sup> datasets in

2. CAF Project: <https://masi.vuse.vanderbilt.edu/workshop2013/index.php/Segmentation-Challenge-Details>



experiments. The resolution of images is  $256 \times 256$ . For each dataset, we randomly take 100 images for training and 50 images for testing. The ADMM-Net is separately learned for each sampling rate such as 10%, 20%, 30%, 40% and 50%. The sampling pattern in  $k$ -space is the commonly used pseudo radial sampling as show in Fig. 8(a). The reconstruction accuracies are reported as the average NMSE and Peak Signal-to-Noise Ratio (PSNR) over the test images. All experiments are performed on a desktop computer with Intel core i7-4790k CPU and GTX1080 GPU. The codes to test and train the deep ADMM-Nets will be available online.

In the following, we first evaluate our approach by comparing two versions of networks. We then investigate the effect of network initialization on reconstruction accuracy. We will also test the impact of different network architectures using different filter numbers (i.e.,  $L$ ), filter sizes (i.e.,  $w_f$ ), iteration numbers in the sub-stages (i.e.,  $N_t$ ) and the number of stages (i.e.,  $N_s$ ). We next compare with conventional compressive sensing MRI methods and also the state-of-the-art methods both qualitatively and quantitatively under different sampling rates. Additionally, we compare with two recent deep learning approaches on the brain data. We finally extent our method to cope with complex-valued MR image and noisy  $k$ -space data reconstruction.

## 5.1 Results of Two Versions of ADMM-Nets

We test and compare the reconstruction performance of Basic-ADMM-Net and Generic-ADMM-Net. We use the brain set with 20% sampling rate to train two kinds of small-scale networks respectively. For Basic-ADMM-Net, we use the basic network settings, i.e.,  $w_f = 3$ ,  $L = 8$ ,  $N_s = 4$  and 15. For Generic-ADMM-Net, we use the similar network settings, i.e.,  $w_f = 3$ ,  $L = 8$ ,  $N_t = 1$ ,  $N_s = 4$  and 15.

TABLE 1  
The result comparisons of different ADMM-Nets on brain data.

Method	RecPF	Basic ( $N_s = 4$ )	Generic ( $N_s = 4$ )	Basic ( $N_s = 15$ )	Generic ( $N_s = 15$ )
NMSE	0.0917	0.0858	0.0751	0.0752	<b>0.0670</b>
PSNR	35.32	35.83	37.04	37.01	<b>38.03</b>

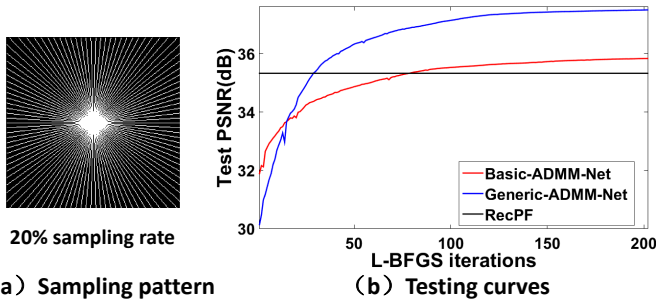


Fig. 8. (a) Pseudo radial sampling pattern with 20% sampling rate. (b) Average test PSNR comparisons between two ADMM-Nets and baseline method RecPF with different L-BFGS iterations.

The average PSNR curves of Basic-ADMM-Net, Generic-ADMM-Net and RecPF method [11] are shown in Fig. 8(b). We use the RecPF method solving a  $TVL_1-L_2$  model by

ADMM algorithm as our baseline method. As can be observed, two ADMM-Nets can get higher performance with increase of the L-BFGS iterations. Furthermore, the Generic-ADMM-Net can converge faster than Basic-ADMM-Net and get the highest precision.

The quantitative comparison results are shown in Tab.1. The results explicitly show that the Generic-ADMM-Net achieves 38.03 dB, 1.02 dB higher than the Basic-ADMM-Net with stage 15. Therefore we adopt the Generic-ADMM-Net as the default network in the following experiments, i.e., the ADMM-Net specifically refers to the Generic-ADMM-Net in the following sections.

## 5.2 Effect of Different Network Initialization

As shown in Sect. 4.1, the network parameters can be initialized by model-based initialization method or random initialization method. We train two networks with these two initializations. In both networks, we set  $w_f = 3$ ,  $L = 8$  and  $N_t = 1$ . The results in Tab. 2 show that the model-based

TABLE 2  
The result comparisons of different initializations.

Method	Model-based ( $N_s = 4$ )	Random ( $N_s = 4$ )	Model-based ( $N_s = 15$ )	Random ( $N_s = 15$ )
NMSE	0.0751	0.0754	<b>0.0670</b>	0.0676
PSNR	37.04	37.01	<b>38.03</b>	37.97

initialization method produces marginally higher reconstruction accuracy than random initialization with the same number of stages. However, the model-based initialization method which uses a set of DCT bases has a limitation on the number of filters in the convolution layers, e.g., 8 filters in size of  $3 \times 3$  (the first DCT basis is discarded), 24 filters in size of  $5 \times 5$  or 48 filters in size of  $7 \times 7$ , etc. We will discuss the effect of the filter number on the reconstruction performance in the following.

## 5.3 Performances of Different Network Architecture

We next test different network architectures by varying the network width (i.e., the number of filters and filter sizes) and network depth (i.e., the number of iterations in the sub-stages and stages). Generally, a wider and deeper network produces higher performance, but costs more computational overhead. We will investigate several configurations of the network structures to best trade-off between reconstruction accuracy and speed for practical demand.

### 5.3.1 Network Width

In this section, we discuss the effect of the network width on the network performance. The width of a network is represented by the number of filters (i.e.,  $L$ ) and the size of filters (i.e.,  $w_f$ ). First, we respectively train ADMM-Nets with 8 filters, 64 filters and 128 filters in size of  $3 \times 3$  in each stage. Three nets share the same network settings which are  $w_f = 3$ ,  $N_s = 4$  and  $N_t = 1$ . The reconstruction results on brain data with 20% sampling rate are shown in Tab. 3. It clearly shows that using more filters could inherently improve the reconstruction quality. The net with 128 filters achieves highest accuracy, e.g., it achieves 0.28 dB higher

TABLE 3  
The result comparisons of different filter numbers on brain data.

Filter Number	L=8	L=64	L=128
NMSE	0.0754	0.0730	<b>0.0701</b>
PSNR	37.01	37.36	<b>37.64</b>
CPU\GPU Time	0.080\0.039s	0.451\0.138s	0.855\0.258s

than the net with 64 filters, but takes around two times in the running time. Then, we justify the effect of different filter sizes in ADMM-Net for reconstruction. We examine three networks with different filter sizes, i.e.,  $w_f = 3$ ,  $w_f = 5$  and  $w_f = 7$ . Other parameters of the network are  $L = 128$ ,  $N_s = 4$  and  $N_t = 1$ . The results in Tab. 4 show that using larger filter size can effectively improve the result. This maybe because larger filter size increases the receptive field of network output modeling higher-order image local correlations. However, the reconstruction speed will be declining by using larger filters. The performance of the network with  $7 \times 7$  filters is only 0.08 dB higher than the network with  $5 \times 5$  filters, but it cost longer testing time.

TABLE 4  
The result comparisons of different filter sizes on brain data.

Filter Size	f=3	f=5	f=7
NMSE	0.0701	0.0657	<b>0.0650</b>
PSNR	37.64	38.21	<b>38.29</b>
CPU\GPU Time	0.855\0.258s	1.584\0.266s	2.646\0.350s

### 5.3.2 Network Depth

We further investigate the effect of different network depths on the network performance. The depth of ADMM-Net depends on the number of iterations in the sub-stages corresponding to the gradient descent iterations in Eqn. (9), and the number of stages corresponding to the iterations in the ADMM algorithm. We first train deeper networks by increasing the number of iterations in the sub-stages (i.e.,  $N_t$ ) in each stage. We train and test ADMM-Nets respectively with  $N_t = 1, 2, 3$ . Other network parameters are set as  $N_s = 3$ ,  $w_f = 5$  and  $L = 128$ . The first four columns of the Tab. 5 show the testing results of ADMM-Nets learned from brain data with 20% sampling rate. We

TABLE 5  
The result comparisons of different sub-stage numbers on brain data

Depth	$N_t=1$ ( $N_s = 3$ )	$N_t=2$ ( $N_s = 3$ )	$N_t=3$ ( $N_s = 3$ )	$N_t=1$ ( $N_s = 4$ )
NMSE	0.0680	0.0670	0.0666	0.0657
PSNR	37.90	38.03	38.08	38.21

find that deeper networks (i.e., having more iterations in sub-stages) with same stage number always result in better accuracy. Then to test the effect of stage number (i.e.,  $N_s$ ), we train deeper networks by adding one stage at each time with other parameters fixed, i.e.,  $N_t = 1$ ,  $w_f = 5$  and  $L = 128$ . Figure 9 shows the average testing NMSE values of the ADMM-Nets using different number of stages

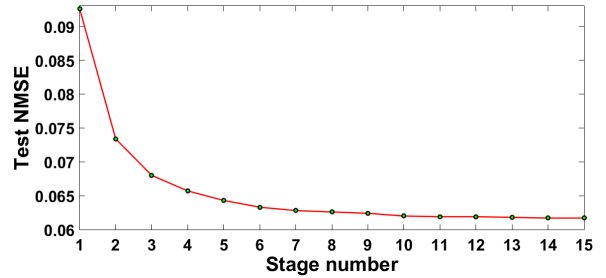


Fig. 9. The testing NMSEs of ADMM-Nets training on brain data with 20% sampling rate using different number of stages.

under the 20% sampling rate by directly joint training. The reconstruction error decreases fast when  $N_s \leq 10$  and marginally decreases when further increasing the number of stages. The testing time of the net increases linearly along with the number of stages.

In the deep ADMM-Net, an increase in the number of parameters by adding one iteration in the sub-stage is similar to an increase by adding one stage. However, from the Tab. 5, the reconstruction accuracy of the ADMM-Net with  $N_t = 1$  and  $N_s = 4$  (i.e., adding one stage) is significantly higher than the ADMM-Net with  $N_t = 2$  and  $N_s = 3$  (i.e., adding one iteration in each sub-stage) and the ADMM-Net with  $N_t = 3$  and  $N_s = 3$  (i.e., adding two iterations in each sub-stage). In this case, adding more stages is more effective than adding more iterations in the sub-stages for achieving superior performance. Therefore we adopt the ADMM-Net with the default network settings, i.e.,  $w_f = 5$ ,  $L = 128$ ,  $N_t = 1$ ,  $N_s = 10$  in the following experiments considering the image reconstruction quality and speed.

### 5.4 Comparison

In this section, we compare our deep ADMM-Net to conventional compressive sensing MRI methods and the state-of-the-art methods on brain data and chest data with different sampling rates. For each sampling rate (i.e., 10%, 20%, 30%, 40%, 50%), we train a specific network for testing.

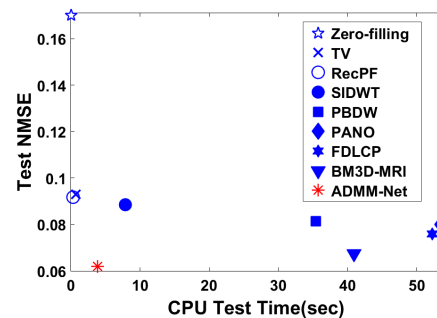


Fig. 10. Scatter plot of NMSEs and CPU test time for different methods.

The conventional methods include Zero-filling [46], TV [3], RecPF [11] and SIDWT<sup>4</sup>. The state-of-the-art methods include PBDW [24] taking advantage of patch-based directional wavelets, PANO [7] making use of similarity of

<sup>4</sup> Rice Wavelet Toolbox: <http://dsp.rice.edu/software/rice-wavelet-toolbox>

TABLE 6  
Performance comparisons on brain data with different sampling rates.

Method	10%		20%		30%		40%		50%		Test Time CPU \ GPU
	NMSE	PSNR	NMSE	PSNR	NMSE	PSNR	NMSE	PSNR	NMSE	PSNR	
Zero-filling [46]	0.2624	26.35	0.1700	29.96	0.1247	32.59	0.0968	34.76	0.0770	36.73	0.001s \ --
TV [3]	0.1539	30.90	0.0929	35.20	0.0673	37.99	0.0534	40.00	0.0440	41.69	0.739s \ --
RecPF [11]	0.1498	30.99	0.0917	35.32	0.0668	38.06	0.0533	40.03	0.0440	41.71	0.311s \ --
SIDWT <sup>3</sup>	0.1564	30.81	0.0885	35.66	0.0620	38.72	0.0484	40.88	0.0393	42.67	7.864s \ --
PBDW [24]	0.1290	32.45	0.0814	36.34	0.0627	38.64	0.0518	40.31	0.0437	41.81	35.364s \ --
PANO [7]	0.1368	31.98	0.0800	36.52	0.0592	39.13	0.0477	41.01	0.0390	42.76	53.478s \ --
FDLCP [29]	0.1257	32.63	0.0759	36.95	0.0592	39.13	0.0500	40.62	0.0428	42.00	52.222s \ --
BM3D-MRI [30]	0.1132	33.53	0.0674	37.98	0.0515	40.33	0.0426	41.99	0.0359	43.47	40.911s \ --
Init-Net <sub>10</sub>	0.2589	26.17	0.1737	29.64	0.1299	32.16	0.1025	34.21	0.0833	36.01	3.827s \ 0.644s
ADMM-Net <sub>10</sub>	<b>0.1082</b>	<b>33.88</b>	<b>0.0620</b>	<b>38.72</b>	<b>0.0480</b>	<b>40.95</b>	<b>0.0395</b>	<b>42.66</b>	<b>0.0328</b>	<b>44.29</b>	3.827s \ 0.644s

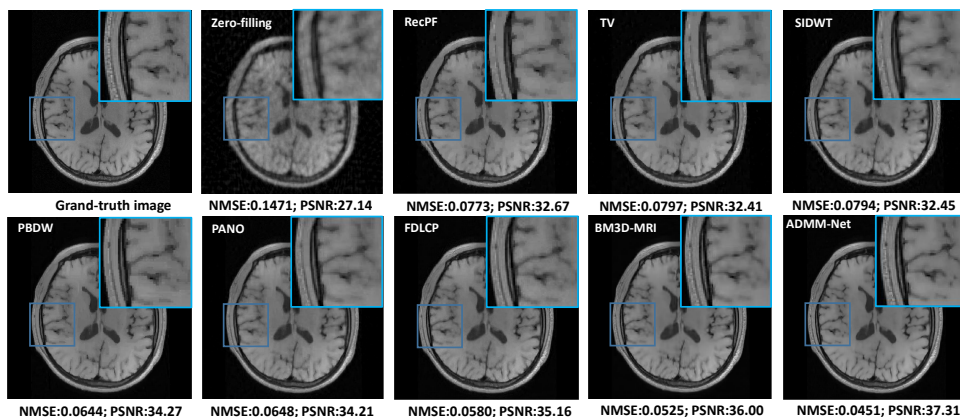


Fig. 11. Examples of reconstruction results on the brain data with 20% sampling rate.

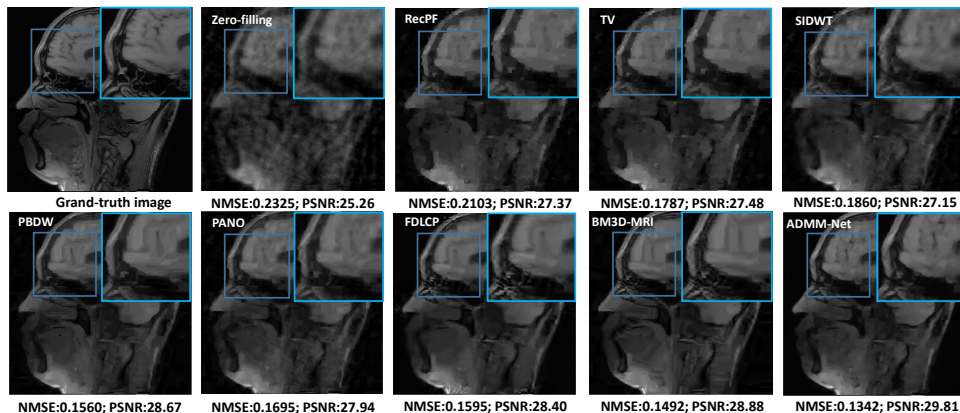


Fig. 12. Examples of reconstruction results on the brain data with 10% sampling rate.

image patches, FDLCP [29] which is a variant of dictionary learning method and BM3D-MRI [30] relying on a well designed BM3D denoiser. For fair comparison, the adjustments of all parameters are according to the same validation set.

Table 6 shows the quantitative results of different methods in different sampling rates on the brain data. Compared with the conventional methods such as Zero-filling, TV, RecPF and SIDWT, our proposed method produces the best quality with comparable reconstruction speed in all

sampling rates. Compared with the state-of-the-art methods such as PBDW, PANO, FDLCP and BM3D-MRI, the ADMM-Net still has the most accurate reconstruction results with fastest computational speed. Specifically, for the sampling rate of 30%, ADMM-Net<sub>10</sub> (i.e. ADMM-Net with 10 stages) outperforms the state-of-the-art methods PANO and FDLCP by 1.82 dB. Moreover, our reconstruction speed is around 13 times faster. ADMM-Net<sub>10</sub> also produces 0.62 dB higher accuracy and runs around 10 times faster in computational

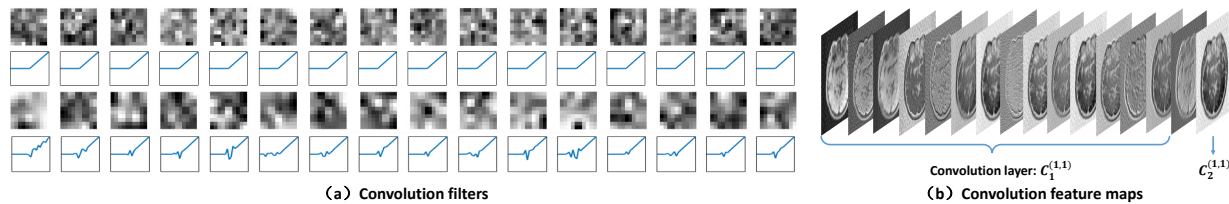


Fig. 13. (a) Examples of learned 16 filters and the corresponding nonlinear transforms. The first two rows are initial filters and nonlinear transforms, the last two rows are trained filters and trained nonlinear transforms. (b) Example feature maps of the convolution layers in the first stage.

TABLE 7  
Comparisons of NMSE and PSNR on chest data with 20% sampling rate.

Method	Zero-filling	TV	RecPF	SIDWT	PBDW	PANO	FDLCP	BM3D-MRI	ADMM-Net <sub>Brain</sub>	ADMM-Net <sub>10</sub>
NMSE	0.1903	0.1019	0.1017	0.0952	0.0884	0.0858	0.0775	0.0694	0.0759	<b>0.0668</b>
PSNR	30.04	35.49	35.51	36.15	36.69	37.01	37.77	38.79	38.00	<b>39.10</b>

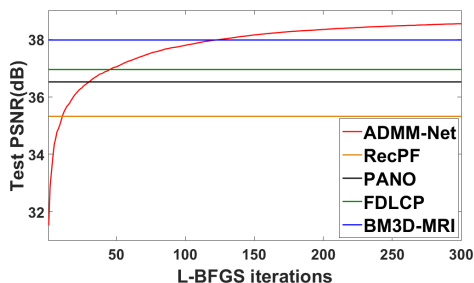


Fig. 14. The testing curves of different methods with L-BFGS iterations.

time than BM3D-MRI method. In Fig. 10, we compare the NMSEs and the average CPU testing time for different methods on 20% brain data using scatter plot. It is easy to observe that our method is the best considering the reconstruction accuracy and running time.

The visual comparisons of 20% and 10% sampling rates are in Fig. 11 and Fig. 12. It clearly show that the proposed network can achieve better reconstruction qualities and preserve the fine image details without obvious artifacts. For the case of low sampling rate (i.e., 10% sampling rate), the ADMM-Net can still reconstruct structural information of the MR image while other methods failed. The examples of the learned nonlinear functions and the filters in the first stage trained on brain data with 20% sampling rate are shown in Fig. 13(a). Each filter and each non-linear function have specific different forms from initialization after training. Figure 13(b) shows an example of relevant convolution feature maps in the first stage, which include different structures and luminance information.

To demonstrate the effectiveness of network training, in Tab. 6, we also present the results of the initialized network (i.e., Init-Net<sub>10</sub>) for ADMM-Net<sub>10</sub>. The network after training produces significantly improved reconstruction accuracy, e.g., PNSR is increased from 29.64 dB to 38.72 dB with sampling rate of 20%. The testing curves of different methods in Fig. 14 show that deep ADMM-Net has powerful abilities of learning, e.g., ADMM-Net<sub>10</sub> outperforms the baseline method (i.e., RecPF) with less 20 L-BFGS iterations, and exceeds state of art methods (i.e., PANO, FDLCP and BM3D-MRI) with less 150 L-BFGS iterations.

We also compare the reconstruction results on chest data with sampling rate of 20%. We test the generalization ability of ADMM-Net by applying the learned net from brain data to chest data. Table 7 shows that our net learned from brain data (ADMM-Net<sub>Brain</sub>) still achieves competitive reconstruction accuracy on chest data, resulting in remarkable a generalization ability. This might be due to that the learned filters and nonlinear transforms are performed over local patches, which are repetitive across different organs. Moreover, the ADMM-Net<sub>10</sub> learned from chest data achieves the best reconstruction accuracy. Thus, the deep ADMM-Net can achieve high performance on MRI reconstruction with different organs.

TABLE 8  
Performance comparisons with deep learning methods on brain data.

Method	Wang et al.	Lee et al.	ADMM-Net
NMSE	0.0973	0.1607	<b>0.0620</b>
PSNR	34.80	30.44	<b>38.72</b>
Training Time	120h	11h	10h

In addition, we compare to several recently proposed deep learning approaches for compressive sensing MRI on brain data with 20% sampling rate. Wang et al. [32] trained a deep convolution network to learn a mapping from down-sampled reconstruction images to fully sampled reconstruction. Then, the output of this network is used as the regularization term in a classical CS-MRI model (i.e. Zero-filling method). Lee et al. [34] adopt U-net to accelerate the data acquisition process, which is a deep deconvolution network with contracting path to learn the residual of MRI reconstruction. We train these two networks on our 100 brain training images which are used for ADMM-Net. We implement the method from Wang et al. based on the *caffe* code from [47], and the U-net from Lee et al. according to the *keras* code<sup>5</sup>. We test the networks on the same 50 brain data with sampling rate of 20%. From the testing results in Tab. 8, we observe that ADMM-Net outperforms these deep learning methods not only for its reconstruction quality but also in terms of the training time. Therefore our

5. retina-unet: <https://github.com/orobix/retina-unet>

TABLE 9  
Comparisons of NMSE and PSNR on complex-valued brain data with different noise level (20% sampling rate).

Method	Zero-filling	TV	RecPF	SIDWT	PBDW	PANO	FDLCP	BM3D-MRI	Complex-ADMM-Net <sub>10</sub>	
NMSE	0.2250	0.1336	0.1320	0.1328	0.1277	0.1300	0.1252	--	<b>0.0988</b>	
PSNR	28.25	32.49	32.54	32.60	32.78	32.88	33.44	--	<b>35.40</b>	
$\sigma = 0.010$	NMSE	0.2250	0.1426	0.1427	0.1415	0.1360	0.1364	0.1354	--	<b>0.0988</b>
	PSNR	28.25	32.06	31.94	32.14	32.30	32.54	32.81	--	<b>35.37</b>
$\sigma = 0.015$	NMSE	0.2250	0.1526	0.1534	0.1500	0.1429	0.1365	0.1463	--	<b>0.0989</b>
	PSNR	28.25	31.54	31.38	31.72	31.99	32.53	32.20	--	<b>35.37</b>

method is superior among these deep learning methods, which include convolution neural network structures.

## 5.5 Complex-valued and Noisy Data Reconstruction

To evaluate the reconstruction performance of the ADMM-Net to cope with complex-valued MR image, we train the Complex-ADMM-Net on the 100 complex-valued brain training data with the sampling rate of 20%. The first two lines in Tab. 9 shows the complex-valued image reconstruction results, where BM3D-MRI method can not reconstruct a complex-valued MR image directly. It is clear that our Complex-ADMM-Net remarkably outperforms all the CS-MRI methods. For the sampling rate of 20%, our method (Complex-ADMM-Net<sub>10</sub>) outperforms the state-of-the-art method FDLCP by 1.96 dB. This might because of the fact that the real and imaginary parts of the data help each other for reconstruction by sharing the network parameters.

Finally, we extent our method to reconstruct k-space data with noise for demonstrating the ability of the ADMM-Net in handling noise. We add the Gaussian white noise to both real and imaginary parts of the training k-space data and testing k-space data. The noisy levels are set into the range of [0, 0.02] for training data, and the noisy levels are set to be 0.010 and 0.015 for testing. We train a Complex-ADMM-Net using noisy training brain data with 20% sampling rate. Table 9 shows the compare reconstruction results of different methods in different noise levels. The hyper-parameters in compared methods are adjusted by noisy validation data whose noisy levels are same with testing data. As a result, the reconstruction performances of the ADMM-Net are mildly influenced by additive noise, e.g., the PSNR is reduced from 35.40 dB to 35.37 dB by adding noise with noise level 0.010 and 0.015. However, the PSNR of state-of-the-art method FDLCP has decreased 1.24 dB since the noise level is 0.015. In summary, the deep ADMM-Net outperforms other CS-MRI methods in term of better reconstruction precision and robustness for noise.

## 6 CONCLUSION

In this work, we proposed two novel deep networks, i.e., Basic-ADMM-Net and Generic-ADMM-Net, for fast compressive sensing MRI. These two nets are deep architectures defined over data flow graphs determined by ADMM algorithms optimizing a general CS-MRI model. This proposed method naturally combines the advantages of model-based approach in easily incorporating domain knowledge, and the deep learning approach in effective parameter learning. Extensive experiments show that these deep nets achieved

higher reconstruction accuracy while keeping the computational efficiency of the ADMM algorithm. As a general framework, the idea that reformulates an ADMM algorithm as a deep network can also be applied to other applications such as image deconvolution, super-resolution, etc.

## ACKNOWLEDGMENTS

The authors would like to thank Prof. Dong Liang at Shenzhen Institutes of Advanced Technology for providing the brain MRI data used in the experiments.

## REFERENCES

- [1] D. Donoho, "Compressed sensing," *IEEE Trans. Information Theory*, vol. 52, no. 4, pp. 1289–1306, 2006.
- [2] M. Lustig, D. Donoho, J. Santos, and J. Pauly, "Compressed sensing mri," *IEEE Trans. Signal Process.*, vol. 25, no. 2, pp. 72–82, 2008.
- [3] M. Lustig, D. Donoho, and J. M. Pauly, "Sparse mri: The application of compressed sensing for rapid mr imaging," *Magnetic Resonance in Medicine*, vol. 58, no. 6, pp. 1182–1195, 2007.
- [4] M. Usman, C. Prieto, T. Schaeffter, and P. Batchelor, "k-t group sparse: a method for accelerating dynamic mri," *Magnetic Resonance in Medicine*, vol. 66, no. 4, pp. 1163–1176, 2011.
- [5] S. Ravishanker and Y. Bresler, "Mr image reconstruction from highly undersampled k-space data by dictionary learning," *IEEE Trans. Medical Imaging*, vol. 30, no. 5, pp. 1028–1041, 2011.
- [6] D. Liang, H. Wang, Y. Chang, and L. Ying, "Sensitivity encoding reconstruction with nonlocal total variation regularization," *Magnetic Resonance in Medicine*, vol. 65, no. 5, pp. 1384–1392, 2011.
- [7] X. Qu, Y. Hou, F. Lam, D. Guo, J. Zhong, and Z. Chen, "Magnetic resonance image reconstruction from undersampled measurements using a patch-based nonlocal operator," *Medical Image Analysis*, vol. 18, no. 6, pp. 843–856, 2014.
- [8] S. Liu, J. Cao, H. Liu, X. Shen, K. Zhang, and P. Wang, "Mri reconstruction using a joint constraint in patch-based total variational framework," *Jour. Visual Communication and Image Representation*, vol. 46, pp. 150–164, 2017.
- [9] W. Yin, S. Osher, D. Goldfarb, and J. Darbon, "Bregman iterative algorithms for  $\ell_1$ -minimization with applications to compressed sensing," *Siam on Imaging Sciences*, vol. 1, no. 1, pp. 143–168, 2008.
- [10] C. Li, W. Yin, H. Jiang, and Y. Zhang, "An efficient augmented lagrangian method with applications to total variation minimization," *Compu. Optimi. and App.*, vol. 56, no. 3, pp. 507–530, 2013.
- [11] J. Yang, Y. Zhang, and W. Yin, "A fast alternating direction method for tvl1-l2 signal reconstruction from partial fourier data," *IEEE Jour. Selec. Topics in Signal Process.*, vol. 4, no. 2, pp. 288–297, 2010.
- [12] S. Ma, W. Yin, Y. Zhang, and A. Chakraborty, "An efficient algorithm for compressed mr imaging using total variation and wavelets," in *Proc. IEEE Conf. Comput. Vis. Pattern Recog.*, pp. 1–8, 2008.
- [13] S. Boyd, N. Parikh, E. Chu, B. Peleato, and J. Eckstein, "Distributed optimization and statistical learning via the alternating direction method of multipliers," *Foundation and Trends in Machine Learning*, vol. 3, no. 1, pp. 1–122, 2011.
- [14] Y. Wang, W. Yin, and J. Zeng, "Global convergence of admm in nonconvex nonsmooth optimization," *arXiv preprint arXiv:1511.06324*, 2015.

- [15] A. Krizhevsky, I. Sutskever, and G. E. Hinton, "Imagenet classification with deep convolutional neural networks," in *Adv. Neural Inf. Process. Syst.*, pp. 1097–1105, 2012.
- [16] J. Schmidhuber, "Deep learning in neural networks: An overview," *Neural Networks*, vol. 61, pp. 85–117, 2014.
- [17] K. Zhang, W. Zuo, Y. Chen, D. Meng, and L. Zhang, "Beyond a gaussian denoiser: Residual learning of deep cnn for image denoising," *IEEE Trans. Image Process.*, 2017.
- [18] J. Kim, J. K. Lee, and K. M. Lee, "Accurate image super-resolution using very deep convolutional networks," in *Proc. IEEE Conf. Comput. Vis. Pattern Recog.*, pp. 1646–1654, 2016.
- [19] Y. Lecun, L. Bottou, Y. Bengio, and P. Haffner, "Gradient-based learning applied to document recognition," *Proceedings of the IEEE*, vol. 86, no. 11, pp. 2278–2324, 1998.
- [20] Y. Yang, J. Sun, H. Li, and X. Zongben, "Deep admm-net for compressive sensing mri," *Adv. Neural Inf. Process. Syst.*, vol. 29, pp. 10–18, 2016.
- [21] J. Huang, C. Chen, and L. Axel, "Fast multi-contrast mri reconstruction," in *Int. Conf. Med. Im. Compu. and Computer-Assisted Intervent.*, pp. 281–288, 2012.
- [22] B. Zhao, J. Haldar, A. Christodoulou, and Z. Liang, "Image reconstruction from highly undersampled (k, t)-space data with joint partial separability and sparsity constraints," *IEEE Trans. Medical Imaging*, vol. 31, no. 9, pp. 1809–1820, 2012.
- [23] K. Block, M. Uecker, and J. Frahm, "Undersampled radial mri with multiple coils: Iterative image reconstruction using a total variation constraint," *Magnetic Resonance in Medicine*, vol. 57, no. 6, pp. 1086–1098, 2007.
- [24] X. Qu, D. Guo, B. Ning, and et al., "Undersampled mri reconstruction with patch-based directional wavelets," *Magnetic resonance imaging*, vol. 30, no. 7, pp. 964–977, 2012.
- [25] S. Gho, Y. Nam, S. Zho, E. Kim, and D. Kim, "Three dimension double inversion recovery gray matter imaging using compressed sensing," *Magnetic Resonance Imaging*, vol. 28, no. 10, p. 1395, 2010.
- [26] X. Peng, L. Ying, Q. Liu, Y. Zhu, Y. Liu, X. Qu, X. Liu, H. Zheng, and D. Liang, "Incorporating reference in parallel imaging and compressed sensing," *Magnetic Resonance in Medicine*, vol. 73, no. 4, pp. 1490–504, 2015.
- [27] S. Wang, J. Liu, P. Xi, D. Pei, Q. Liu, and L. Dong, "Two-layer tight frame sparsifying model for compressed sensing magnetic resonance imaging," *Biom. Research Int.*, vol. 2016, pp. 1–7, 2016.
- [28] S. Babacan, X. Peng, X. P. Wang, and M. Do, "Reference-guided sparsifying transform design for compressive sensing mri," in *Proc. IEEE Int. Conf. Med. and Biolo. Society*, pp. 5718–5721, 2011.
- [29] Z. Zhan, J.-F. Cai, D. Guo, Y. Liu, Z. Chen, and X. Qu, "Fast multi-class dictionaries learning with geometrical directions in mri reconstruction," *IEEE Trans. Biomedical Engineering*, 2016.
- [30] E. Eksioğlu, "Decoupled algorithm for mri reconstruction using nonlocal block matching model: Bm3d-mri," *Journal of Mathematical Imaging and Vision*, pp. 1–11, 2016.
- [31] J. Huang and F. Yang, "Compressed magnetic resonance imaging based on wavelet sparsity and nonlocal total variation," in *IEEE Int. Symposium on Biomedical Imaging*, pp. 968–971, 2012.
- [32] S. Wang, Z. Su, L. Ying, and X. Peng, "Accelerating magnetic resonance imaging via deep learning," in *Proc. IEEE Int. Symposium on Biomedical Imaging*, pp. 514–517, 2016.
- [33] J. Schlemper, J. Caballero, J. V. Hajnal, A. Price, and D. Rueckert, "A deep cascade of convolutional neural networks for mr image reconstruction," *arXiv preprint arXiv:1703.00555*, 2017.
- [34] L. Dongwook, Y. Jaejun, and C. Jong, "Deep residual learning for compressed sensing mri," *IEEE Int. Sympo. on Biome. Imag.*, 2017.
- [35] K. Gregor and Y. LeCun, "Learning fast approximations of sparse coding," in *Proc. 27th Int. Conf. Machine Learning*, pp. 399–406, 2010.
- [36] U. Schmidt and S. Roth, "Shrinkage fields for effective image restoration," in *Proc. IEEE Conf. Comput. Vis. Pattern Recog.*, pp. 2774–2781, 2014.
- [37] S. Jian and X. Zongben, "Color image denoising via discriminatively learned iterative shrinkage," *IEEE Trans. Image Process.*, vol. 24, no. 11, pp. 4148–4159, 2015.
- [38] J. R. Hershey, J. L. Roux, and F. Weninger, "Deep unfolding: Model-based inspiration of novel deep architectures," *arXiv preprint arXiv:1409.2574*, 2014.
- [39] Y. Li and S. Osher, "Coordinate descent optimization for  $l_1$  minimization with application to compressed sensing; a greedy algorithm," *Inverse Prob. & Imag.*, vol. 3, no. 3, pp. 487–503, 2009.
- [40] I. Daubechies, M. Defrise, and C. De Mol, "An iterative thresholding algorithm for linear inverse problems with a sparsity constraint," *Commu. Pure & Applied Mathematics*, vol. 57, no. 11, pp. 1413–1457, 2003.
- [41] Y. Chen and T. Pock, "On learning optimized reaction diffusion processes for effective image restoration," in *Proc. IEEE Conf. Comput. Vis. Pattern Recog.*, pp. 87–90, 2015.
- [42] S. D. Hammernik K, Knoll F, "Learning a variational model for compressed sensing mri reconstruction," in *Proc. Int. Society of Magnetic Resonance in Medicine*, 2016.
- [43] B. Xin, Y. Wang, W. Gao, and D. Wipf, "Maximal sparsity with deep networks?," in *Adv. Neural Inf. Process. Syst.*, pp. 4340–4348, 2016.
- [44] F. Bach, R. Jenatton, J. Mairal, and G. Obozinski, "Optimization with sparsity-inducing penalties," *Foundations and Trends in Machine Learning*, vol. 4, no. 1, pp. 1–106, 2012.
- [45] K. He, X. Zhang, S. Ren, and J. Sun, "Delving deep into rectifiers: Surpassing human-level performance on imagenet classification," in *Proc. IEEE Conf. Comput. Vis. Pattern Recog.*, pp. 1026–1034, 2015.
- [46] M. Bernstein, S. Fain, and S. Riederer, "Effect of windowing and zero-filled reconstruction of mri data on spatial resolution and acquisition strategy," *Magnetic Resonance Imaging*, vol. 14, no. 3, pp. 270–280, 2001.
- [47] C. Dong, C. C. Loy, K. He, and X. Tang, "Image super-resolution using deep convolutional networks," *IEEE Trans. Pattern Analysis & Machine Intelligence*, vol. 38, no. 2, pp. 295–307, 2016.